Coversheet
2021/07/29

Crystallographic preferred orientation, seismic velocity and anisotropy in roofing slates

Víctor Cárdenes

Department of Geology University of Oviedo, Spain

Marco A. Lopez-Sanchez

Géosciences Montpellier – CNRS & Université de Montpellier, France

Fabrice Barou

Géosciences Montpellier – CNRS & Université de Montpellier, France

Javier Olona

Department of Geology University of Oviedo, Spain

Sergio Llana-Fúnez

Department of Geology University of Oviedo, Spain

corresponding author: cardenesvictor@uniovi.es

Crystallographic preferred orientation, seismic velocity and anisotropy in roofing slates

Víctor Cárdenes[a]*, Marco A. Lopez-Sanchez[b], Fabrice Barou[b], Javier Olona[a], Sergio Llana- Fúnez[a]

[a]*Geology Department, Oviedo University, C/ Jesús Arias de Velasco s/n, 33005 Oviedo, Asturias, Spain*
[b]*Géosciences Montpellier, Université de Montpellier & CNRS, Place E. Bataillon, 34095 Cedex 5, Montpellier, France*

Corresponding author
E-mail: cardenesvictor@uniovi.es
Tel.: +34 985 10 33 84

Abstract

Mica-rich rocks (shales, slates, schists) are a major and significant component of the continental crust. They are often characterized by a strong seismic anisotropy, a key factor in the seismic interpretation of the architecture of the continental crust. Roofing slates are a group of natural rocks used in construction that must possess a continuous and undeformed slaty cleavage. This makes roofing slates an exceptional benchmark to study the relation between the rock microstructure and the development of seismic anisotropy in single-foliated low-grade slates. Direct measurements of seismic velocities using an ultrasonic wavemeter at room conditions were done on eight cubic samples from active quarries in the NW Iberian Peninsula. Seismic velocities were also calculated using the Hill averaging method from crystallographic preferred orientation (CPO) maps of slate-forming minerals on the same sample blocks using electron backscatter diffraction (EBSD), achieving unprecedented coverages of up to 87%. The seismic velocities estimated by both methods are similar parallel to the slaty cleavage but much slower using direct measures in the axial direction, producing anisotropies for Vp and Vs1 up to 7 and 5 times higher than the calculated velocities. The results are indicative of the highly anisotropic contribution that cracks, pores and fractures have in single-foliated slates, given the strong shape fabric that the rocks present. The samples selected also show that not all slates exhibit near-transverse isotropy, as it has been commonly assumed.

Keywords: *Slate; Crystallographic Preferred Orientation; Tectonite; Seismic velocity; Seismic anisotropy; Phyllosilicates*

1. Introduction

What is a slate? For Fettes et al. (2011) a slate is an "ultrafine or very fine-grained metamorphic rock displaying slaty cleavage". In turn, slaty cleavage is a "type of continuous cleavage in which the individual grains are too small to be seen by the unaided eye". This definition makes clear that slate is a rock defined by structural (cleavage) and textural (grain size) criteria, resulting from the combination of deformation and metamorphism of fine-grained pelitic sediments. Slaty cleavage results from the growth of paragenetic phyllosilicates during metamorphism (Kameda et al., 2011), in addition to the structural rearrangement of primary minerals during associated regional deformation. The typical mineral assembly for slates is quartz, feldspar, mica and chlorite, frequently with carbonates and iron sulphides as accessory minerals. Slate is thus a rock that combines sedimentary relict features with newly developed metamorphic and tectonic structures, representing the transition from diagenesis to low-grade metamorphism in the context of regional deformation.

There are two main structures in a typical slate: sedimentary fabric, or bedding, (S0) and a tectonic fabric, i.e. the slaty cleavage (S1). The intersection of these two structures creates a third one, the intersection lineation (L1). Dominant slate-forming minerals have a very strong shape orientation, defining S1. This feature can be seen using any microscopy technique, gives slate its characteristic fissility, and makes it very appealing for construction since it is easy to split into regular blocks. The arrangement of these structural features determine the classification of slates as an S-tectonite (Passchier and Trouw, 2005). However, when the process of sedimentation involves the formation of a fabric due to the geometric orientation of particles during compaction and diagenetic growth, and bears some type of fabric determined by the arrangement of particles during compaction and diagenesis, the intersection between S0 and S1 can result in a linear fabric, i.e. from S-tectonite (stack of plane-shapes) to L-tectonite (stack of pencil-shapes). Generally for phyllitic rocks, a flattening strain will generate S-tectonites while plane strain (such as simple shear) SL-tectonites with transverse anisotropy (Ji et al., 2013b; Ji et al., 2015; Shao et al., 2014).

The presence of slates in many orogenic belts, together with its remarkable structural anisotropy, make this rock an exceptional proxy for the study of the relations between rock microstructure and seismic anisotropy. With microstructure, we refer here to the size, shape and spatial interrelationship between the grains (Fettes et al., 2011). The strong crystallographic control in the development of the shape of mica grains, implicitly involves also crystallographic preferred orientation.

When a slate outcrop has little or no deformation and the rock is homogeneous, it can be used to produce roofing slate shingles, a construction material with very specific requirements (Cárdenes et al., 2014). Roofing slate shingles must be thin, flat and regular. Roofing slate outcrops can therefore provide homogeneous samples of fine and undeformed slate, which is perfect for the study of crystallographic-preferred orientations (CPO). The CPO can be determined using Electron Backscatter Diffraction (EBSD) or Synchrotron X-ray Microtomography (S-MCT). Each of these two techniques has its pros and cons. With EBSD, it is possible to link directly microstructure and CPO. Samples require a high degree of polishing so the beam can index as many grains as possible, avoiding grain boundaries that might interfere with indexation (Prior et al., 2009). On the other hand, S-MCT scans a given volume of rock, discriminating among mineral components via differences in their attenuation coefficient (μ), and finding the CPO for the whole rock volume. For this technique, sample preparation is easier than for EBSD; usually, a rock cylinder measuring just a few millimetres will suffice. However, the resolution depends on the sample volume (the lower the resolution, the better), so it is best if the cylinders have diameters of around 2 mm, which can be

rather arduous to obtain, depending on sample integrity. Both techniques produce comparable CPO data (e.g. Wenk et al., 2020).

There are many examples of CPO determination and its relationship to other physical parameters of deformed metamorphic rocks, e.g. marbles (Austin et al., 2014), gneisses (Ivankina et al., 2017), eclogites (Keppler, 2018; Park and Jung, 2019; Renedo et al., 2015), mylonites (Elyaszadeh et al., 2018; Fazio et al., 2017), amphibolites (Cao et al., 2010; Ji et al., 2013b; Ko and Jung, 2015; Mainprice and Nicolas, 1989), peridotites (Ben Ismail and Mainprice, 1998; Jung, 2011; Kang and Jung, 2019; Nicolas et al., 1973), and serpentinites (Dilissen et al., 2018; Ji et al., 2013a; Jung, 2011). All these rocks excluding slates have grain sizes from medium to coarse. Due to the economic interest of shales, CPO has also been fairly studied in fine-grained rocks below and at the boundary of the low-grade metamorphic scale (e.g. Lonardelli et al., 2007; Sayers, 2005; Vasin et al., 2013). The next lithology with increasing metamorphism, slate, has been the subject of significantly less research despite being a major component of the upper-middle crust.

Sintubin (1994) studied the orientation of phyllosilicates in argillites from the Stavelot-Venn Massif, finding that mineral orientations are the result of regional deformation. Wenk et al. (2017) have studied CPO in slates using S-MCT, finding a very strong CPO for phyllosilicates (chlorite and mica). Recently, Wenk et al. (2020) have published a detailed review of the fabric of slates using high-energy X-ray diffraction and EBSD concluding that the extremely high alignment of the phyllosilicates can be attributed to growth and dissolution processes maintained during low-grade metamorphism. The weak development of CPO in quartz in these rocks suggests that intracrystalline plasticity is not the main deformation mechanism at play in this mineral. Dissolution-precipitation processes have been proposed to explain the lack of CPO and the strong shape fabric of quartz (e.g. Engelder et al., 1981). On the other hand, phyllosilicates are prone to deformation by slippage, and then usually rearrange with deformation. Saur et al. (2020) have applied high-resolution X-ray computed tomography (XCT) coupled with X-ray spectroscopy (EDS) to the determination of Shape-Preferred Orientation (SPO) of grains in a metamorphic succession from shales to slates, ranging from a cleavage-free domain to a pencil-cleavage domain, and to a slaty-cleavage domain. They found grain alignment and rotation with increasing strain, but also a difference in SPO depending on grain composition (quartz and calcite). Quartz grains in these conditions are rigid and not prone to deform internally, while calcite grains present deformation and recrystallization features.

Regarding mechanical behaviour, slate is considered a significantly homogeneous rock in terms of rock mechanics. Mechanical properties in foliated rocks are primarily determined by the angle S1/S0 (ß) (Chlupáčová et al., 2003; Godfrey et al., 2000). In slates from the same outcrops as those in this study, Rodríguez-Sastre and Calleja (2006) found that this angle determines seismic velocities, Young's modulus and the Poisson coefficient, all of these values being 2–3 times lower when ß approaches 0° than when ß = 90°.

The sources of seismic anisotropy in crustal rocks depend on several factors. In the upper crust, anisotropy is mainly controlled by the development of fractures (e.g. Crampin, 1984), the regional stress field (e.g. Boness and Zoback, 2006) or structures (e.g. Acevedo et al., 2020). At greater depths/pressures (>200 MPa), the crystallographic preferred orientation and the elastic properties of the minerals composing the rock are the main sources of seismic anisotropy as porosity and microcracks close at high confining pressure over geological times. Indeed, Guo et al. (2014) have found that with increasing confining pressure seismic velocity increases while anisotropy decreases, as the axial and transverse seismic velocity values approach. These authors explained this as a result of the closure of microcracks parallel to S1, which at low confining pressures hinder wave propagation across the main foliation, while transverse propagation maintains similar values. Similar results have been found in shales (i.e. Lu et al., 2019; Vasin et al., 2013). Although the

progress of metamorphic reactions with depth leads to reduced porosity, the exhumation processes cause new microcracks in the slate massifs losing their original seismic properties (Akker et al., 2018). An alternative way to constrain seismic properties at depth, avoiding the effect of microcracks, is to model the seismic properties using averaging schemes from the measured CPO and the modal amount of mineral phases (Almqvist and Mainprice, 2017; Mainprice and Nicolas, 1989). These averaging schemes require knowledge of the elastic properties of the minerals that make up the rocks to be modelled.

Here, we have studied several roofing slate samples from different active Spanish quarries by using EBSD data and calculating seismic velocities and anisotropy using the Voigt-Reuss-Hill averaging (VRH) method. We compare these results with seismic wave velocities measured using an ultrasonic pulse meter at room conditions.

2. Materials and methods

2.1. Sampling and slate properties

The slate blocks were selected from active roofing slate quarries located in several areas in the NW Iberian Peninsula (Fig. 1). The slate district is based in a low to medium grade metamorphic belt formed during the development of the Variscan orogen, mostly Carboniferous in age in this part of the mountain belt (Dallmeyer et al., 1997). In the area, the widespread and regional tectonic foliation is a slaty cleavage that forms in relation to near isoclinal, often recumbent, large folds (e.g. Pérez-Estaún et al., 1991). This dominant fabric is often crenulated by a secondary regional tectonic fabric in relation to upright open folds (e.g. Bastida et al., 2010). Roofing slate quarries either target areas where rocks only develop the regional slaty cleavage or where secondary tectonic fabrics are homoaxial to the earlier slaty cleavage, and avoid locations where the angle between two superimposing tectonic foliations is oblique, as crenulations would prevent the extraction of planar slate shingles.
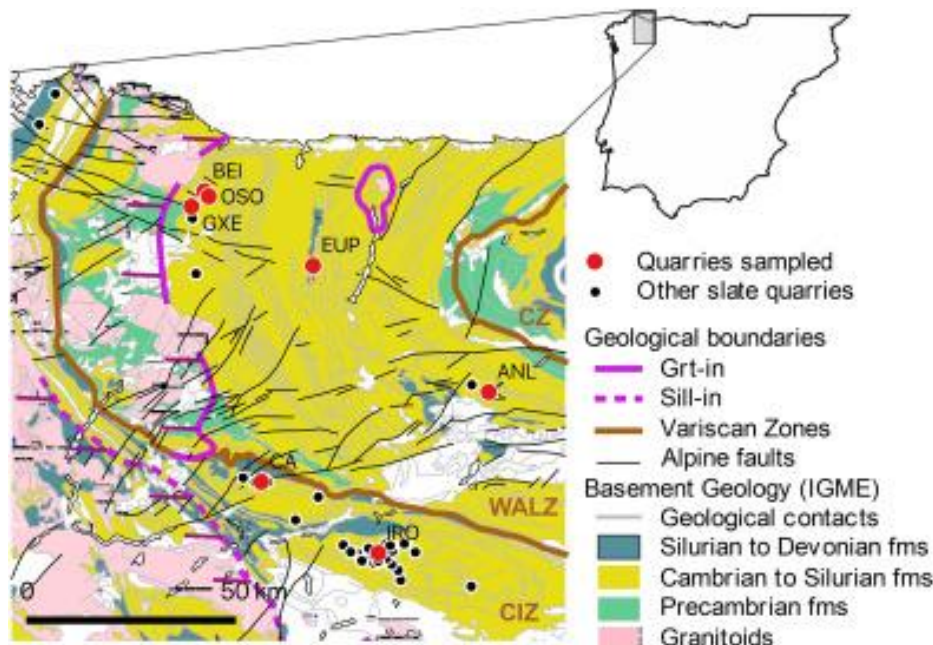

Fig. 1. Geological context of slate quarries in NW Spain, showing the location of samples used in this study. The geological map is extracted from the Geological Map of Spain at 1:1,000,000 (www.igme.es). CZ, Cantabrian Zone; WALZ, West-Asturian Leonese Zone; and, CIZ, Central-Iberian Zone (after Julivert, 1971).

In addition, the roofing slate industry requires outcrops that are large, homogeneous and free of fractures. Quarries of this special type of ornamental rock are therefore perfect for obtaining fine-grained (10–30 µm) and compact samples of slate with a perfectly developed slaty cleavage S1

(Cárdenes et al., 2014). The samples were thus large, clean blocks of slate taken directly off the production line, several metres below the surface into the unaltered rock massif. Slate shingles are split along S1, crossing the oblique S0 planes (Fig. 2). The intersection of these two planes, S0 and S1, creates the lineation L1, which is used during the manufacturing process to define the length of the slate shingles, optimizing their mechanical performance. The blocks are therefore cut along this direction, which helped us to orient the structures of the slate. Due to the high degree of fissility required to exfoliate 6–8 mm thick shingles, most of the slate extracted from the quarry is rejected (85–90%, Cárdenes et al. (2014) due to heterogeneities such as kink-bands, quartz veins, or joints, accumulated since the Variscan orogeny through to the Alpine orogeny. All the blocks sampled were taken from the production chain, which means they were suitable for exfoliation. Each of these blocks weighed between 50 and 70 kg. However, a detailed examination highlighted some heterogeneities in samples ANL and especially GXE, which do not affect exfoliation but could influence our results. Sample ANL was found to have two well-differentiated parts, one composed of a homogeneous and clean slate, and the other containing visible sandy beds defining S0. To study the influence of these sandy beds, this sample was divided into two sub-samples, ANL-I and ANL-II. On the other hand, GXE presented two families of microscopic recrystallized quartz levels, one parallel and the other oblique to S1.
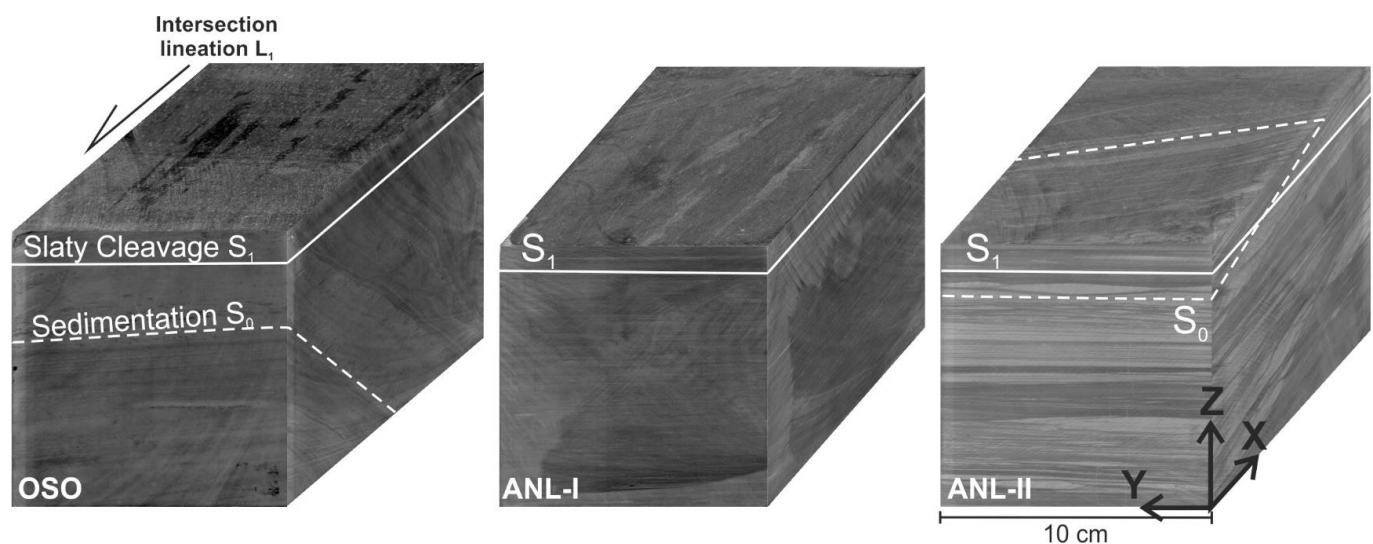

Fig. 2. Examples of 10 cm side cubes used for seismic wave velocities determination. Plane XY is parallel to S1. Plane ZY is normal to S1 and parallel to the intersection lineation L1. Plane YZ is normal to S1 and L1. Some samples (ANL-I and ANL-II) show bedding (S0) nearly parallel to S1, while others (OSO) present angles higher than 45° between these two structures.

All blocks were kept at room temperature with average humidity conditions (50–70%) until they were sawed into 10 cm edge cubes. Lineation was visible in all of the slate blocks, marked by S0 and S1 planes (Fig. 2). As standard in structural geology, the reference frame used has the Z direction perpendicular to the foliation, the X direction parallel to the lineation, and the Y direction contained in the foliation plane and perpendicular to X (Fig. 2).

2.2. Microstructure and petrological analysis

The characterization of the microstructure and mineralogy was carried out using transmitted-light microscopy (on the three main planes), SEM-BSE, electron backscatter diffraction (EBSD) and energy-dispersive X-ray spectroscopy (EDX) on the XZ planes. X-ray diffraction and fluorescence were used for the description of the bulk mineral and chemical composition, respectively. All analyses except EBSD and EDX were performed at the Scientific Services of the University of Oviedo.

2.2.1. Electron backscatter diffraction (EBSD) data acquisition

A small slab (2 × 2 cm) was extracted for each sample, using the XZ plane for the EBSD analysis. To protect the slab before the polishing process, each slab was encapsulated with epoxy resin at room pressure without penetrating the pore system but merely supporting it. The samples were then polished with diamond paste and finished by polishing with colloidal silica in a VibroMet Polisher. EBSD and Energy-dispersive X-ray spectroscopy (EDX) maps were acquired with a CamScan X500-FE CrystalProbe SEM at Géosciences Montpellier (France) to determine the crystallographic-preferred orientations and mineral phase content. Samples were not carbon-coated. Operating conditions for EBSD acquisition were an accelerating voltage of 20 kV and a working distance of 24–25 mm under low vacuum conditions (~5 Pa). EBSD patterns were indexed using HKL Technology's AZtec v3.2 software at rates of ~40 Hz. The local maps had step sizes (spatial resolution) within the range of 0.7–0.8 μm and covering areas from 505 × 617 to 1737 × 1411 μm². Angular resolutions are better than 0.5 degrees. Indexing rates in raw maps ranged between 72 and 87% of the surface analyzed (Fig. 2).

2.2.2. Electron backscatter diffraction (EBSD) data processing

Post-acquisition data treatment was performed using MTEX toolbox v5.2 (Mainprice et al., 2014) and in-house MATLAB codes, provided as Supplementary Material. Orientation data with MAD above 1.3 were not considered, and wild spikes were removed. Grains were then segmented using a Voronoi decomposition algorithm with the misorientation threshold set to 10°. CPO are presented in upper-hemisphere contour pole figures representing volume/area-weighted orientations. CPO strength for each mineral phase and specific crystallographic element was characterized with the J-index, which ranges from one (uniform distribution) to infinite (a single orientation) (Mainprice et al., 2014), and presented as misorientation profiles with a random orientation distribution for reference.

2.3. Prediction of seismic properties from rock composition and CPO

We used MTEX v5.2 and the procedures described in (Mainprice et al., 2011) to predict seismic velocities and anisotropy based on the Voight-Reuss-Hill (VRH) averaging method (Hill, 1952; Reuss, 1929; Voigt, 1928). More specifically, we considered the CPO and the relative volumetric contribution of the rock-forming mineral phases (quartz, muscovite, chlorite and albite). Single-crystal properties and references used are listed in Table 1 and detailed in the codes provided as Supplementary Material. Transversal and axial seismic anisotropy for Vp and Vs1 was calculated using the expression $200 \times (V_{max} - V_{min}) / (V_{max} + V_{min})$ on two perpendicular planes, while for shear wave splitting the expression $100 \times Vs1_i - Vs2_i / mean(Vs1)$ was used. To gauge how mica CPO and mica content affects the seismic properties of the slates, we defined a new proxy called the normalized J-index of micas. The estimation of this proxy value is done in two steps:

1. First combining the J-index of the micas (muscovite and chlorite) weighting their J-index values to their relative content. This procedure has the advantage of avoiding possible bias caused by micas with extreme J-index values and low volumetric representation.
2. Then, this J-index value is normalized by weighting it to the total mica content of the slate so that the proxy allows the comparison of slates with different mica content.

Table 1. *Summary of single-crystal properties and references used for the VRH averaging method.*

Mineral	Density (g/cm³)	Elastic constants	Stiffness tensor
Quartz	2.65	McSkimin et al. (1965)	
Low albite	2.623	Brown et al. (2006)	
Muscovite	2.83	Vaughan and Guggenheim (1986)	
Chlorite	2.628	Joswig et al. (1989)	Bayuk et al. (2007)

2.4. Laboratory measurements using ultrasonic waves

Seismic wave velocities Vp and Vs1 were measured in the cubes at room conditions using a portable ultrasonic pulse velocity meter (Pundit PL-2) with 500 KHz transducers. Velocities were measured at least three times for each principal direction in the cubic samples and then averaged using the arithmetic mean.

3. Results

3.1. Mineral content and microfabric

Mineral content (Table 2) and chemical compositions (see Supplementary Table 1) are typical for slates. Quartz, albite, chlorite and muscovite are the main constituents. Other mineral phases (anatase, ilmenite, hydroxyl, apatite, calcite, zircon or pyrrhotite) do not exceed 3.6% in total. The mica content of the samples varies between 28 and 56%, with Chl/Ms. ratios between 1.29 and 0.58 (Table 2).

Table 2. Mineral content (%).

sample	quartz	muscovite	anatase	albite	chlorite	hydroxylapatite	ilmenite	calcite	zircon	pyrrhotite	Chl/Ms ratio	% of mica
ANL II	48.9	19.6	1.3	3.9	25.2	0.7	0.4	---	---	---	1.29	44.7
ANL II	47.3	24.3	1.5	4.2	21.6	0.7	0.4	---	---	---	0.89	45.9
BEI	29.8	27.6	0.3	24.1	16.1	0.8	0.4	0.9	---	---	0.58	43.6
CA	47.2	25.5	1.3	0.8	24.2	0.6	0.4	---	---	---	0.95	49.7
EUP	45.5	16.9	0.4	22.1	10.9	0.8	---	2.2	0.4	0.7	0.65	27.8
GXE	56.1	16.4	0.8	13.7	12.2	0.7	---	---	---	---	0.74	28.6
IRO	26.7	26.7	1.3	14.7	29.3	1.3	---	---	---	---	1.10	56.0
OSO	36.7	24.0	0.4	25.4	12.1	0.5	1.0	---	---	---	0.51	36.1

*Recalculated from EBSD data assuming that non-indexed pixels are equally distributed across the different recognised phases.

The mineral arrangement is strongly dominated by the slaty cleavage, being similar across samples (Fig. 2, Fig. 3). The arrangement of the main mineral phases looks similar on XZ (lineation-parallel) and YZ (lineation-normal) sections. Quartz grains tend to be elongated except in pressure shadows in which they appear as a crystal mosaic. The chlorite blasts appear elongated with S1. Two types of muscovite can be distinguished: primary muscovite with sizes below 2 μm forming most of the dark matrix, and secondary (metamorphic) muscovite with larger (up to 80 μm in length) and an acicular habit. The fabric is lepidoblastic, characteristic of roofing slates (Cárdenes et al., 2014).
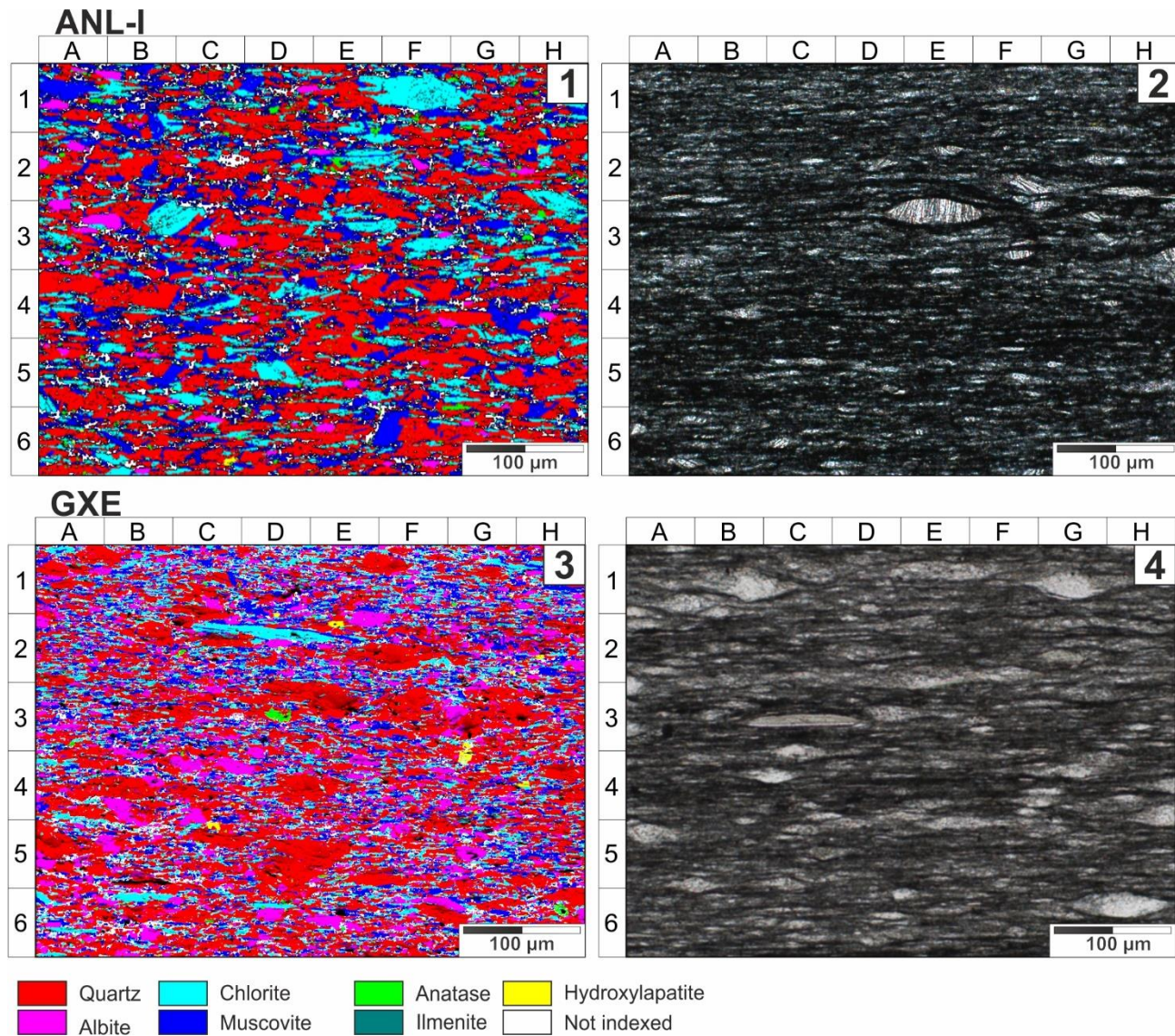
Fig. 3. EBSD mineral phase maps (2−1 and 2−3) versus transmitted light optical microscope (2−2 and 2−4). EBSD and microscope images do not correspond to the same area. All images correspond to plane XZ.

3.2. Crystallographic preferred orientation

The high quality of the samples and the careful preparation protocol allowed us to obtain EBSD indexing rates within the range 70% to 87%, which is remarkably high for rocks with this amount of phyllosilicates. The CPO patterns in micas can be reduced into two types (Fig. 4). Samples BEI, CA, EUP and GXE have a planar pattern, with (001) planes lying parallel to the foliation plane and the crystallographic axes [010] and [100] placed at random within the foliation plane. Samples ANL-I, ANL-II, OSO and IRO with a planar/linear pattern where the crystallographic axes [100] and [010] develop a maximum within the foliation plane. The (001) pole figure maxima for muscovite and chlorite have exceptionally strong alignments up to 50 and 80 multiples of a uniform distribution, respectively, using a half-width of 5 degrees (Fig. 4). Anatase also displays a strong CPO with (001) pole figure maxima perpendicular to the foliation plane and the crystallographic axes [001] and [010] lying within the foliation plane (Fig. 5). By contrast, quartz and feldspar show very weak or completely random CPOs (Fig. 5). The misorientation angle distribution for quartz, muscovite and chlorite illustrated in Fig. 6 highlights the randomness of quartz CPO in contrast to that of micas. The strength of the quartz and albite CPO, measured by the index J, yield values close to a random distribution (J = 1), especially for quartz. Indeed, the misorientation angle distribution for quartz follows the theoretical random reference profile (Fig. 6). J-index in the micas reveals highly variable CPO strengths across samples, ranging from 5 to 40 for chlorite and from 3.8 to 21 for muscovite (see

Fig. 2 in Supplementary material). Except for samples ANL and IRO, the distributions of the misorientation angles in micas show a nearly flat distribution except for the most extreme values (Fig. 6).
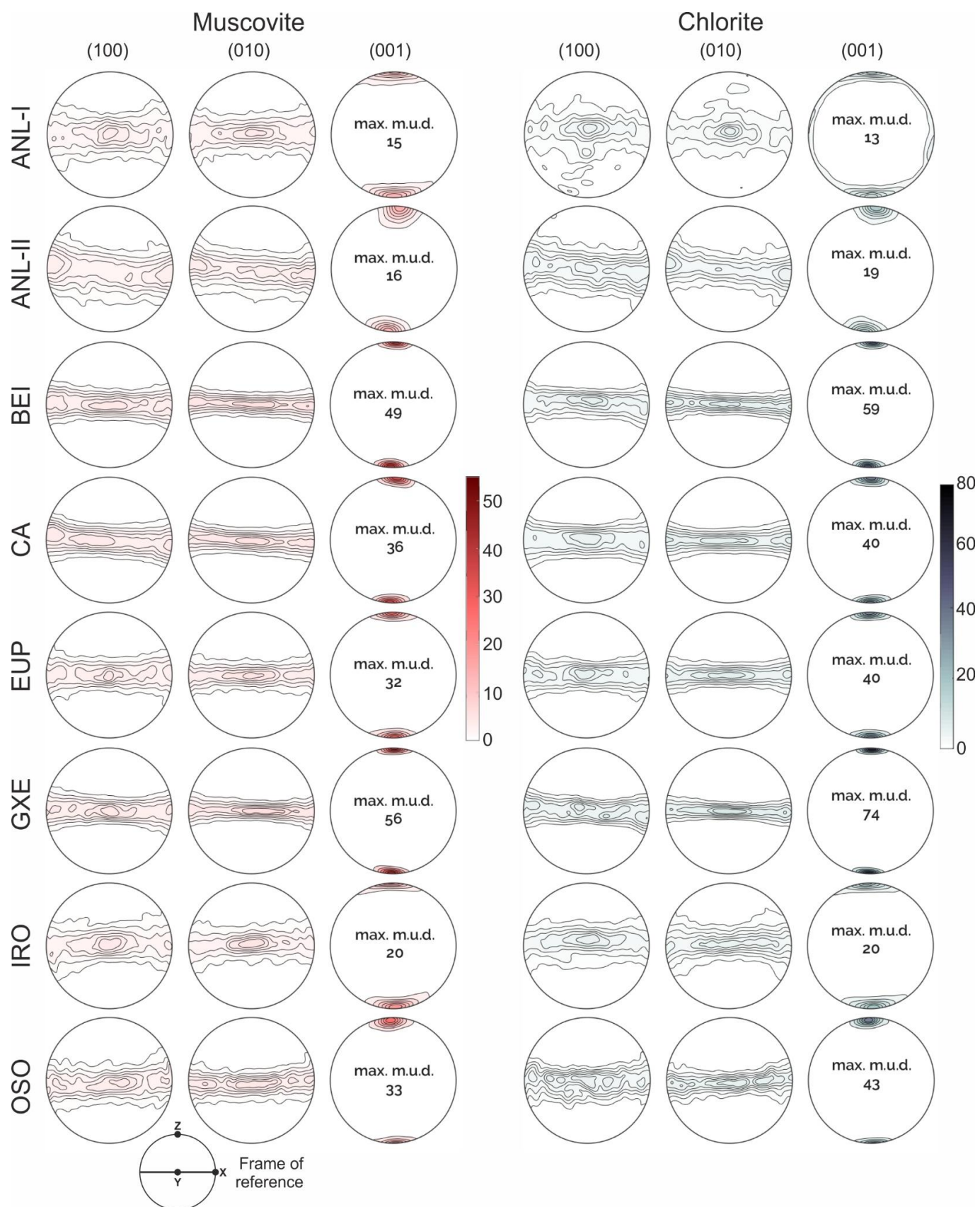

Fig. 4. Muscovite and chlorite CPO pole figures. The CPO is strong for all the samples but for ANL-I and ANL-II, which have some scattering in the plane (010). Upper hemisphere equal-area projections, contours in multiples of uniform distribution (half-width 5°). Linear intensity scale is the same for each mineral phase.
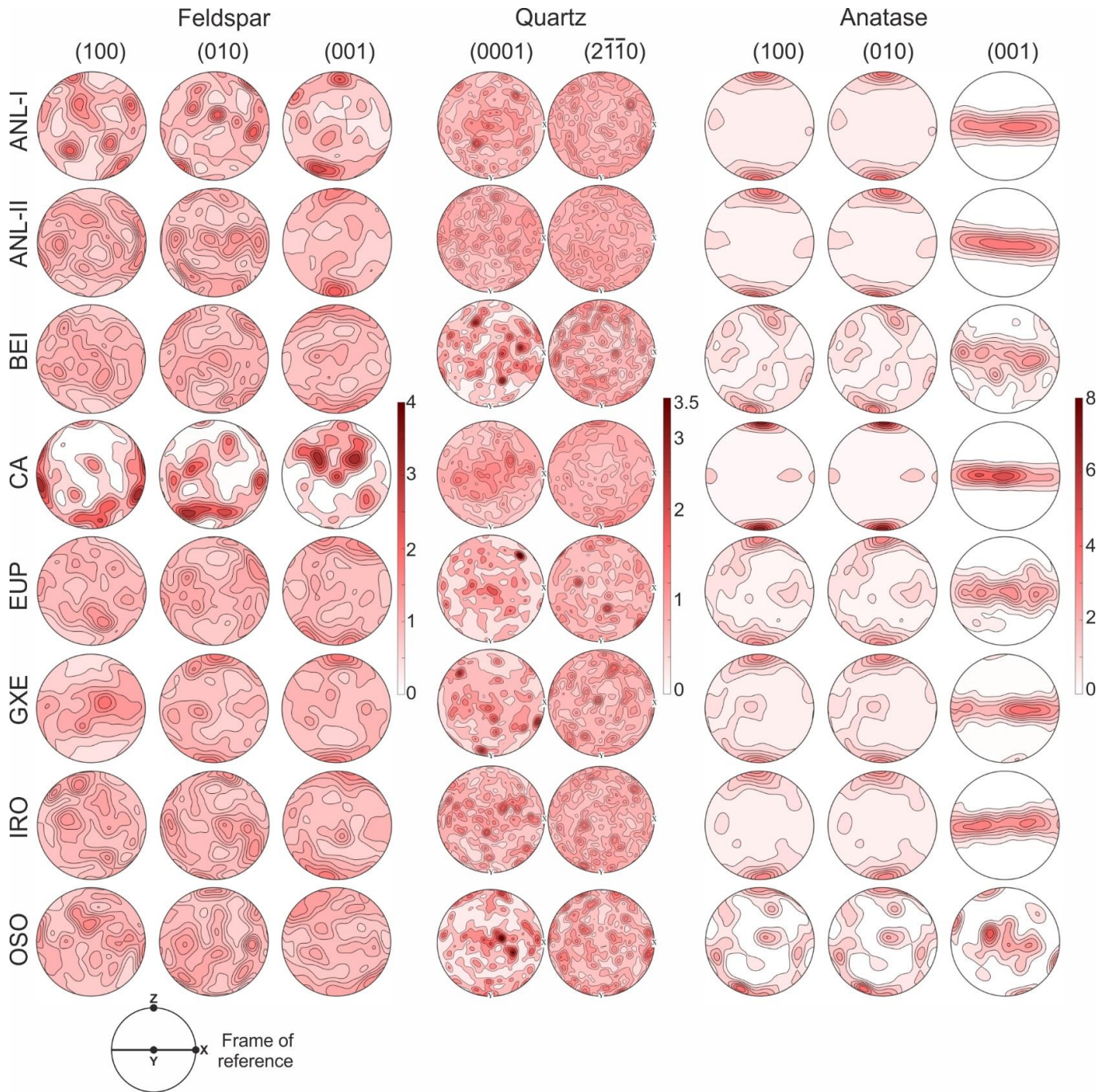
Fig. 5. Feldspar, quartz and anatase CPO pole figures. Feldspar and quartz show random to very weak CPOs. Anatase has a strong CPO in samples ANL-I, ANL-II, CA, GXE and IRO, being slightly weaker in BEI and EUP and weak in OSO, likely due to the small number of anatase grains in this sample (n = 64). Upper hemisphere equal-area projections, contours in multiples of a uniform distribution (half-width 10°). The linear intensity scale is the same for each mineral phase.
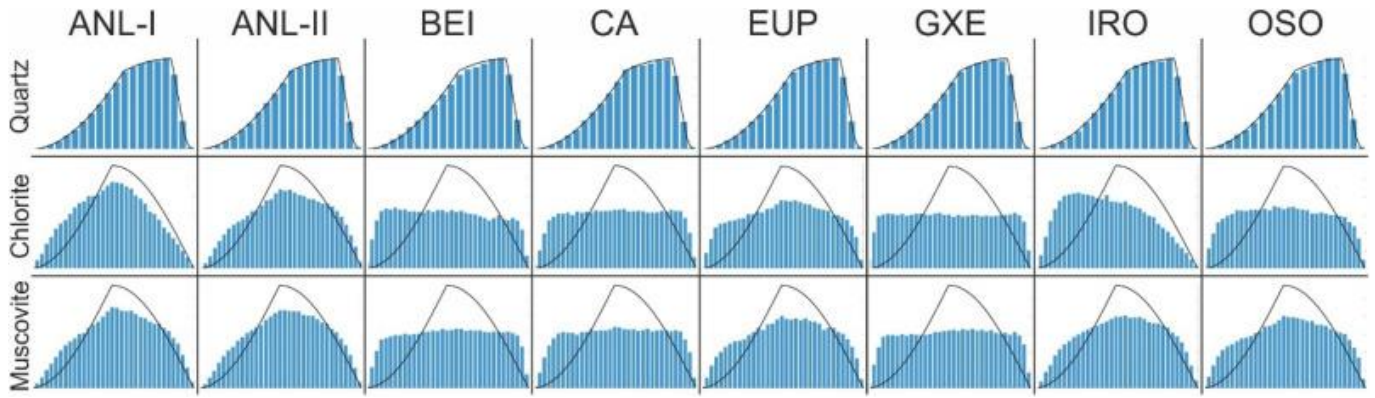
Fig. 6. Misorientation angle histograms for the main mineral phases. The black line shows the theoretical random profile for each phase. Quartz shows no crystallographic preferred orientation, in opposition to the strong crystallographic preferred orientation of chlorite and muscovite.

3.3. Seismic velocities and anisotropy

The seismic velocities were obtained using two different methods: calculated by the Hill averaging method and measured in the 10 cm edge cubes with the ultrasonic wave meter at room conditions.

3.3.1. Laboratory measurements

Seismic velocities measured with the ultrasonic wave meter along principal structural directions (X, Y, Z) are provided in Table 3. Vp normal to the foliation plane (Z direction) varies considerably across samples, between 3.330 and 5.063 km/s, while in the transversal (X and Y) directions show rather similar values, between 6.174 and 6.727 km/s. Vs1 normal to the foliation plane vary slightly, between 2.5 and 2.873 km/s axially and between 3.916 and 4.265 km/s for X and Y directions. Overall, Vp and Vs1 velocities transmitting normal to the foliation vary between 50 and 75% of the average within the foliation, producing extreme axial anisotropies (up to 66%) and transverse anisotropies below 1.7% excepting for Vp in samples ANL and IRO (Table 3).

Table 3. Ultrasonic wave velocities measured at room pressure along main directions.

sample	Vp (km/s)			Axial anis. (%)	Trans. anis. (%)	Vs1 (km/s)			Axial anis. (%)	Trans. anis. (%)	number of measures	density
	X	Y	Z			X	Y	Z				
ANL (I & II)	6.174	6.416	4.205	41.6	3.8	3.916	3.928	2.500	44.4	0.3	9	2.76
BEI	6.561	6.671	3.516	61.9	1.7	4.142	4.124	2.751	39.9	0.4	12	2.77
CA	6.656	6.727	5.063	28.2	1.1	4.265	4.235	2.873	38.3	0.7	10	2.78
EUP	6.575	6.655	3.330	66.6	1.2	4.089	4.109	2.659	42.8	0.5	8	2.76
GXE	6.653	6.709	4.685	35.5	0.8	4.189	4.197	2.605	46.8	0.2	8	2.80
IRO	6.276	6.721	4.013	50.5	6.8	3.876	3.840	2.873	28.8	0.9	14	2.79
OSO	6.501	6.630	3.679	57.3	2.0	4.052	4.051	2.745	38.4	0.0	11	2.75

3.3.2. Seismic velocities using the VRH averaging method and comparison with laboratory velocities

Calculated seismic velocities and anisotropy using the VRH averaging method are provided in Fig. 7 and Table 4. Briefly, Vp and Vs1 anisotropy vary between 13.6 ± 3.0 and $12.9 \pm 3.3\%$ (CI 95%) respectively, while shear wave splitting and Vp/Vs1 vary 13.0 ± 3.3 and $11.5 \pm 2.4\%$ respectively. The distribution of the maximum directions for the propagation of the seismic waves (Fig. 7) reveals the preferential alignment following the plane of the foliation, i.e. the slaty cleavage. Fig. 7, Fig. 8 also show that there are two types of slates in terms of Vp and Vs1. Those with nearly isotropic transverse

P-wave velocities (~1.5%) and those (ANL and IRO) with transversal anisotropies up to 5.3% (6.85% using the ultrasonic pulse transmission).
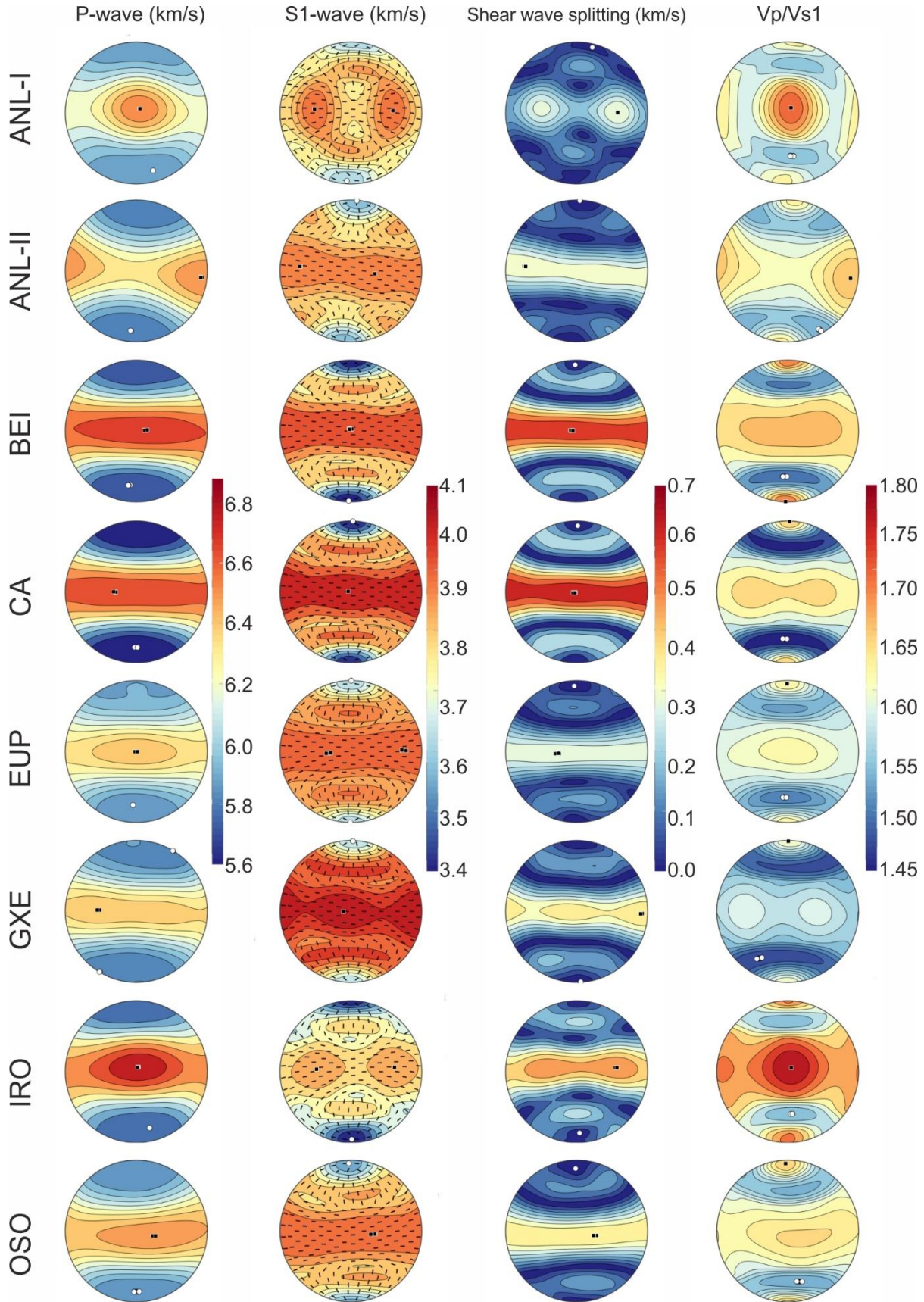

Fig. 7. Contoured equal-area polar plots (upper hemisphere) illustrating seismic velocities and anisotropy as a function of orientation: Vp, Vs1, shear wave splitting and Vp/Vs1, using the Hill averaging method. For the shear wave splitting the velocity difference between Vs1 and Vs2 is provided. All units in km/s except for Vp/Vs1 which is a ratio.

Table 4. Seismic wave properties of slates using the Hill averaging method.

sample	Vp			Vs1			Shear Wave Splitting			Vp/Vs1		
	max (km/s)	min (km/s)	anisotropy (%)	max (km/s)	min (km/s)	anisotropy (%)	max diff. (km/s)	min diff. (km/s)	max. anisotropy (%)	max (km/s)	min (km/s)	anisotropy (%)
ANL-I	6.592	5.874	11.5	3.950	3.616	8.8	0.365	0.005	9.5	1.731	1.540	11.7
ANL-II	6.571	5.809	12.3	3.942	3.561	10.2	0.384	0.003	10.0	1.675	1.529	9.1
BEI	6.787	5.717	17.1	4.030	3.362	18.1	0.697	0.007	18.0	1.719	1.490	14.3
CA	6.758	5.600	18.7	4.097	3.382	19.1	0.737	0.006	19.1	1.672	1.442	14.7
EUP	6.466	5.862	9.8	3.974	3.628	9.1	0.362	0.005	9.3	1.634	1.500	8.6
GXE	6.453	5.815	10.4	4.080	3.636	11.5	0.455	0.003	11.5	1.620	1.467	9.9
IRO	6.880	5.766	17.6	3.913	3.373	14.8	0.571	0.009	15.2	1.791	1.536	15.3
OSO	6.562	5.851	11.4	3.971	3.531	11.7	0.447	0.004	11.5	1.664	1.526	8.6
arith. mean *			13.6 ± 3.00			12.91 ± 3.33			13.01 ± 3.26			11.52 ± 2.40
conf. Int.**			7.03 - 20.17			5.61 - 20.21			5.86 - 20.16			6.26 - 16.79

*with standard error for the mean at 95% of certainty (t-student distribution)

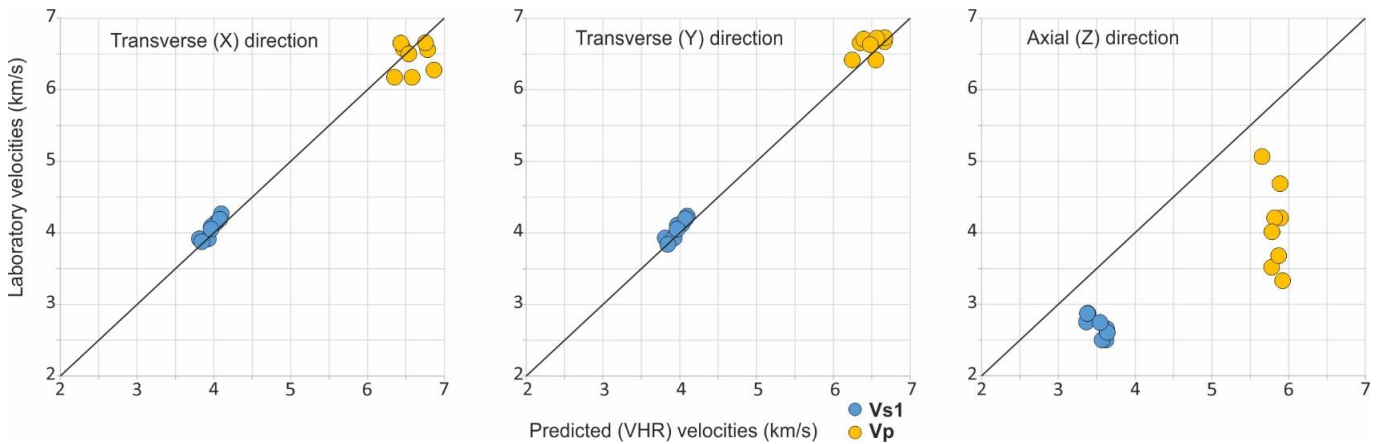**confidence interval for the spread of the data at 95% of certainty (1.96*SD)

Fig. 8. Vp and Vs1 laboratory vs. calculated (Hill averaging method) velocities as a function of the principal directions.

A comparison between the measured (laboratory) and calculated (using the Hill average) Vp and Vs1 seismic velocities along the principal structural directions reveal that they are similar along the foliation (transversal) plane but markedly faster normal to the foliation (Z-direction) (Fig. 9). It is also noteworthy that the Vp calculated using the Hill average yields very consistent values among samples, of ~5.8 km/s, whereas the Vp measured in the laboratory under room conditions vary greatly, between 3.3 and 5.1 km/s. For Vs1, the calculated velocities are faster than those measured in the laboratory, but they appear clustered rather than scattered (i.e. laboratory measures provide rather similar velocities across samples).
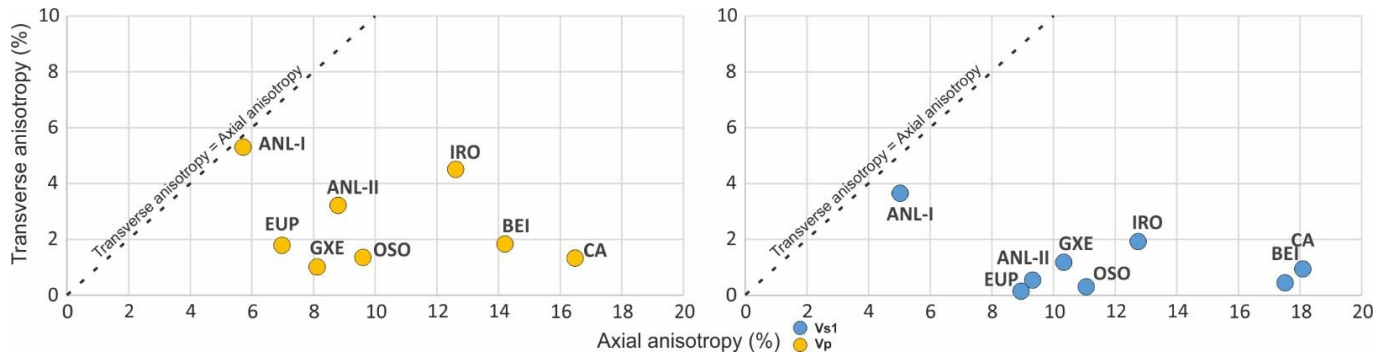
Fig. 9. Transverse (parallel to cleavage plane) vs Axial (perpendicular to cleavage plane) seismic anisotropy for Vp and Vs1 in the samples studied.

3.3.3. Relationship between CPO strength of micas and seismic anisotropy

Table 5 provides the values for the normalized mica CPO strength to test whether the seismic properties of the slates mainly depend on the strength of the mica CPO and their proportion. Overall, there is a positive correlation between this proxy parameter and the seismic anisotropy (Fig. 10). This correlation is weak (R-squared < 0.52) but becomes noticeable when the sample GXE is ignored, especially for Vs1 and SWS (R-squared up to 0.87).

Table 5. Mica CPO strength (J-index) values and the Normalized Mica J-index strength parameter.

| sample | Muscovite | | Chlorite | | J-index of micas* | Modal proportion of mica | Norm. Mica CPO strengh** |
	J-index	relative proportion	J-index	relative proportion			
ANL-I	4.373	0.438	8.061	0.563	6.448	0.444	2.866
ANL-II	3.845	0.529	5.255	0.471	4.509	0.459	2.071
BEI	15.738	0.632	25.955	0.368	19.502	0.437	8.518
CA	12.820	0.513	15.426	0.487	14.090	0.494	6.956
EUP	8.833	0.607	14.886	0.393	11.209	0.278	3.115
GXE	21.140	0.574	40.010	0.426	29.176	0.286	8.353
IRO	6.313	0.476	11.883	0.524	9.231	0.560	5.169
OSO	8.995	0.664	18.277	0.336	12.113	0.361	4.368

*Weighted J-index for micas using $(J_{Ms} \times proportion) + (J_{Chl} \times proportion)$

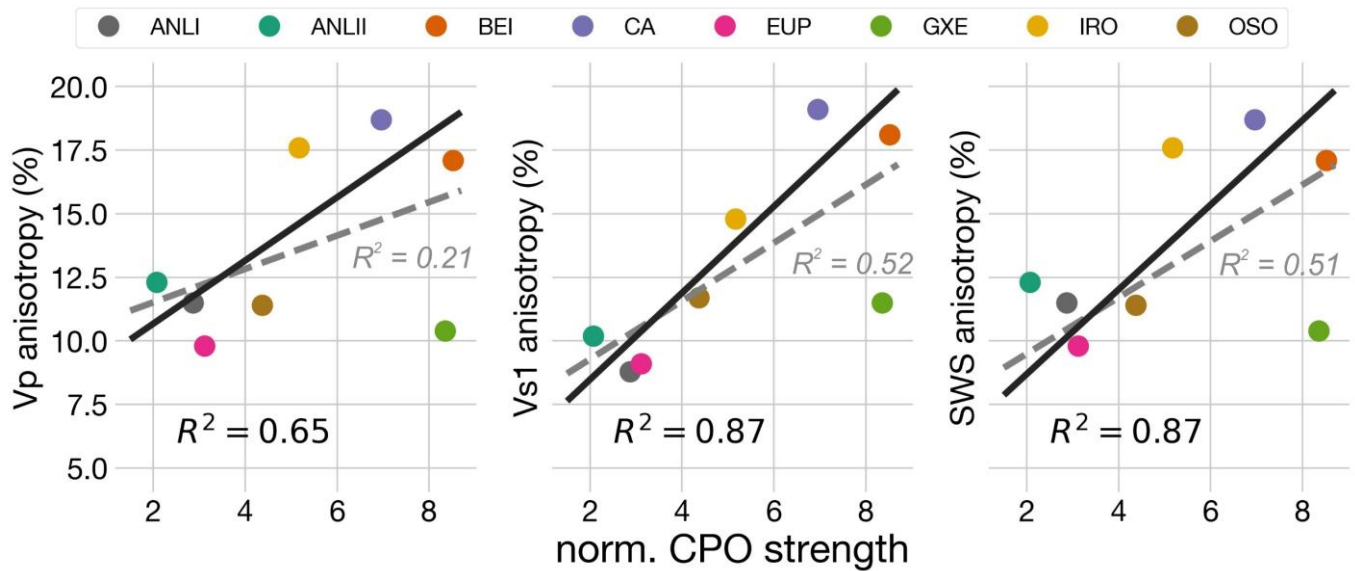**Weighted to the total mica content of the rock.

Fig. 10. Correlation between seismic anisotropies and the Normalized Mica CPO Strength proxy. In dashed grey linear correlation results considering all samples. In black, linear correlation results ignoring the sample GXE.

4. Discussion

4.1. Crystallographic preferred orientation

We have analyzed a heterogeneous set of low-grade single-foliated slates. Overall, CPO patterns are rather similar across samples for the different mineral phases. Thus, for the micas, the (001) planes lie parallel to the slaty cleavage that vary from 12 multiples of a uniform distribution to exceptionally strong alignments up to 80. Quartz and albite show a very weak or random CPO. These observations agree with those previously observed in other single-foliated slates (Crampin, 1984; Fettes et al., 2011; Godfrey et al., 2000; Keppler, 2018; Mainprice and Nicolas, 1989; Valcke et al., 2006; Sintubin, 1994; Wenk et al., 2017, Wenk et al., 2020).

Some of the samples studied, however, show unusual or previously unreported features. Firstly, a few of them show planar/linear CPO patterns where the crystallographic axes [100] and [010] develop a maximum within the cleavage plane. This contrasts with the other samples studied here but, most importantly, to previous studies where single-foliated slates show no a-axis CPO at all; i.e. it is commonly assumed that in such slates there is rotational freedom over the (001) pole of the mica platelets within the cleavage plane (e.g. Wenk et al., 2020 and references therein). The other observation to highlight, previously unreported, is the strong CPO developed in anatase. In terms of morphology, planar-shaped minerals are prone to align when subjected to deformation, either by rotation or by growth under stress or both, while round-shaped minerals do not exhibit any arrangement at all. The growth of phyllosilicates during deformation imposes a sharp control on orientation (e.g. Wenk et al., 2020). This is supported by the strong CPO displayed by anatase, a secondary mineral that also grows during metamorphism and deformation, and which has not been reported before. Most prior studies have focused on shales, revealing a strong CPO due to sedimentary deposition and compaction (Valcke et al., 2006). In our samples, the strong CPO found in secondary chlorites and anatase suggests a preferred mineral growth throughout metamorphism in relation to an early phase of Variscan deformation, S1 (e.g. Dallmeyer et al., 1997).

Anatase is the low-temperature polymorph of rutile (TiO2), and usually grows as isolated and euhedral crystals. The CPO of anatase suggests that it grew during the formation of the main tectonic fabric and associated metamorphism. A literature review on anatase grown during low-degree metamorphism yielded just only one reference (Meszaros et al., 2019), according to which the needle-shaped crystals of anatase have a random distribution in slates. However, this study does not

estimate the CPO; rather, the data about anatase orientation comes from petrological (shape) determination. As pointed out before, previous studies have found similar planar fabrics in shales, developed due to the mechanical deposition of phyllosilicates in stagnant water, and, to a lesser extent, to diagenetic growth. The prograde of metamorphism in the context of regional deformation involves preferential growth of phyllosilicates supported by dissolution.

4.2. Effect of the microstructure in seismic anisotropy of single-foliated slates

The seismic anisotropy (Hill average) data in the samples studied agree with previous estimates in slates and biotite gneisses using various approaches (Fig. 11). For example, Guo et al. (2014) estimated anisotropies in slates using ultrasonic measurements at confining pressures >0.15 GPa of ~13% (Vp) and ~17% (Vs1), both values within the range found in our samples and thus within the confidence interval at 95% established with our dataset assuming that they are normally distributed. Valcke et al. (2006) provided anisotropies of 11.1% (Vp) and 9.8% (SWS) using the same VRH averaging approach in a chlorite-bearing slate, similar to those estimated in our less anisotropic samples (ANL-I and EUP). The average Vp anisotropy of our dataset is also similar to those values estimated in biotite gneiss samples, either those using ultrasonic measurements at high pressure (0.6 GPa) at 13.2% (Kern et al., 2015) or by using the self-consistent averaging method at 12.6% (Wenk, 2012).

Ultrasonic measurements in shales and slates at pressures below 0.1 GPa provided anisotropy values that are higher than the 95% confidence intervals derived with the Hill averaging method for both Vp (20–30%) and Vs1 (19–35%) (e.g. Johnston and Christensen, 1995). These anisotropy values based on ultrasonic measurements at low pressures are strongly conditioned by extrinsic factors, such as the presence of cracks and porosity (Guo et al., 2014; Seront et al. 1993). Indeed, ultrasonic measurements taken under room pressure conditions on our sample set provide very high anisotropy values, in line with the values found in shales, and a strong scattering for both Vp (28.2 to 61.9%) and Vs1 (38.3 to 46.8%). It is noteworthy that the discrepancy between Hill- and ultrasonic-based seismic speeds occur in directions other than those contained in the slaty cleavage (Fig. 8), which explains the large difference of anisotropy values between both methods. This observation also agrees with that found by Guo et al. (2014) on low-grade slates based on ultrasonic measurements at high pressures.

Since the VRH averaging method ignores all extrinsic factors affecting the elastic wave speeds, this indicates that the effect of fractures, cracks and/or pores is very anisotropic in single-foliated slates. Other heterogeneities such as cracks filled with quartz and sandy laminations oblique to S1 (Fig. 2) might play a role. However, given the obliquity of these long-range heterogeneities to the cleavage, they should affect seismic velocities in all directions, which conflicts with our observations and suggests microcracks and pores as primary sources for this effect since they are always present. In conclusion, seismic anisotropy estimates based on the ultrasonic pulse transmission method measured under room conditions in slates are not reliable for depth seismic surveys, where the effect of pressure and low-grade metamorphism will suppress or attenuate the extreme seismic anisotropy found in shales or exhumed low-grade slates. However, such extreme anisotropy values might potentially be used for low-grade slate prospecting under surface or subsurface conditions.
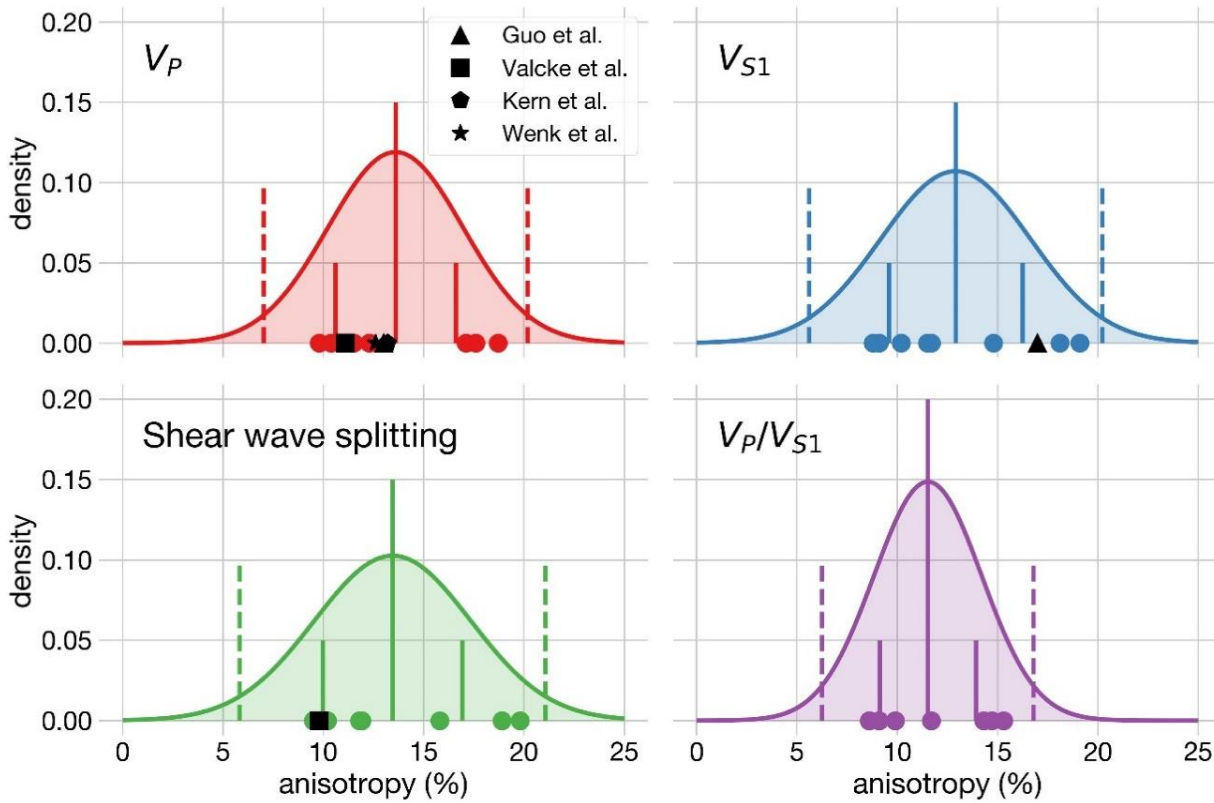
Fig. 11. Comparison between the seismic anisotropy values obtained using the Hill averaging method and previous studies in slates (Valcke et al., 2006; Guo et al., 2014) and biotitic gneisses (Kern et al., 2009; Wenk, 2012). The fitted normal distributions (n = 8) show the arithmetic mean (large solid line), the confidence interval for the mean (short solid lines), and the confidence intervals for the data spread (dashed lines), both at a 95% certainty level.

4.3. The role of CPO on the symmetry of the seismic velocities

As illustrated in Fig. 9, a key finding of the study is that three slate samples show transversal anisotropies up to 5.3% (6.85% with ultrasonic measures). The low transversal anisotropy values (<<2%) found in most slates agree with previous studies (e.g. Guo et al., 2014 and references therein) and thus with the common assumption of considering shales/slates (regarded as S-tectonites) as a nearly transverse isotropic elastic material. The samples with transverse anisotropy values >2% are those with the lowest CPO strength (J-index) values and with planar/linear CPO patterns in our dataset. The latter feature suggests a plane strain genetic mechanism for the formation of these slates (e.g. Ji et al., 2015; Shao et al., 2014). This finding has important consequences as some parameters used to quantify elastic anisotropy in shales/slates, such as the Thomsen parameters (ε, γ, δ) (Thomsen, 1986) or the W200 and W400 coefficients (e.g. Sayers, 2005), requires the medium to be transversely isotropic.

Previous studies in shales and synthetic mica-rich aggregates found a positive correlation between the strength of the CPO in the micas and the seismic anisotropy (Johnston and Christensen, 1995; Naus-Thijssen et al., 2011b). The modal content in micas is also considered a major factor, as other major mineral phases, such as quartz, do not usually develop a strong CPO and hence they contribute to decreasing the bulk seismic anisotropy (Naus-Thijssen et al., 2011a). We tested these assumptions using a proxy that considers both the CPO intensity of the micas (measured as the J-index) and the mica modal content and found a positive correlation between the seismic anisotropy and the proxy (Fig. 10). As previously indicated, the proxy fails to predict a robust linear correlation if the GXE sample is taken into account, i.e. the linear model only explains half or less of the data (R-squared ≤ 52). If the sample GXE is ignored, the linear model provides R-squared values between 64 and 88% with all p-values indicating significant positive linear correlations and suggesting that both

factors play a major role. Compared to others, sample GXE has the particularity of having a significant proportion of heterogeneities and a large proportion of recrystallized quartz aggregates, which contrasts with a very strong CPO mica strength. These features might explain their out-of-trend seismic behaviour.

5. Conclusions

The most significant findings in our study between microstructure and seismic anisotropy can be summarized as follows:

1. In slates with a single tectonic foliation, the inconsistency between the seismic velocities estimated with the VRH averaging method (Hill average) and those measured in the laboratory at room conditions occurs in the direction normal to the foliation, but not parallel to it. This explains the extreme seismic anisotropy observed when measured under room conditions, between 5 and 7 times higher than that estimated using the Hill averaging method. Likewise, it indicates that the effect of aligned microcracks, fractures and porosity (the main extrinsic factors) on seismic velocities is highly anisotropic in single-foliated slates. This prevents extrapolation of estimates based on ultrasonic measurements in slates at room conditions for regional seismic surveys at depths where microcracks no longer cause these effect due to their sealing. However, in the study of seismic anisotropy in the upper crust, direct measurement of seismic velocities has the potential to identify the orientation of anisotropy due to microcracks.

2. Overall, there is a positive linear correlation between mica's CPO strength (normalized with the modal content of micas) and seismic anisotropy. This suggests that these two features are the main sources of seismic anisotropy in single-foliated slates.

3. Anatase shows a strong crystallographic preferred orientation in slates suggesting a preferred mineral growth during metamorphism.

4. Not all slates exhibit near-transverse isotropy, as has been commonly assumed; we have found some elastic anisotropy values as high as ~5–6%. This should be taken into account when using proxy parameters to quantify elastic anisotropy that depends on the transverse isotropy of the medium.

Supplementary material

https://www-sciencedirect-com.insu.bib.cnrs.fr/sdfe/pdf/download/S0040195121000998/attachments

References

Acevedo, J., Fernández-Viejo, G., Llana-Fúnez, S., López-Fernández, C., Olona, J., 2020. Upper-Crustal Seismic Anisotropy in the Cantabrian Mountains (North Spain) from Shear-Wave Splitting and Ambient Noise Interferometry Analysis. Seismol. Res. Lett., 92, 421-436

Akker, I.V., Kaufmann, J., Desbois, G., Klaver, J., Urai, J.L., Berger, A., Herwegh, M., 2018. Multiscale porosity changes along the pro- and retrograde deformation path: an example from Alpine slates. Solid Earth 9, 1141-1156.

Almqvist, B.S.G., Mainprice, D., 2017. Seismic properties and anisotropy of the continental crust: Predictions based on mineral texture and rock microstructure. Reviews of Geophysics 55, 367-433.

Austin, N., Evans, B., Rybacki, E., Dresen, G., 2014. Strength evolution and the development of crystallographic preferred orientation during deformation of two-phase marbles. Tectonophysics 631, 14-28.

Ben Ismail, W., Mainprice, D., 1998. An olivine fabric database: an overview of upper mantle fabrics and seismic anisotropy. Tectonophysics 296, 145-157.

Boness, N.L., Zoback, M.D., 2006. Mapping stress and structurally controlled crustal shear velocity anisotropy in California. Geology 34, 825-828.

Cao, S.Y., Liu, J.L., Leiss, B., 2010. Orientation-related deformation mechanisms of naturally deformed amphibole in amphibolite mylonites from the Diancang Shan, SW Yunnan, China. Journal of Structural Geology 32, 606-622.

Cárdenes, V., Rubio-Ordóñez, Á., Wichert, J., Cnudde, J.P., Cnudde, V., 2014. Petrography of roofing slates. Earth-Science Reviews 138, 435-453.

Chlupáčová, M., Skácelová, Z., Nehybka, V.r., 2003. P-Wave anisotropy of rocks from the seismic area in Western Bohemia. Journal of Geodynamics 35, 45-57.

Crampin, S., 1984. Effective anisotropic elastic constants for wave propagation through cracked solids. Geophysical Journal International 76, 135-145.

Dilissen, N., Hidas, K., Garrido, C.J., Kahl, W.A., Sanchez-Vizcaino, V.L., Padron-Navarta, J.A., 2018. Textural evolution during high-pressure dehydration of serpentinite to peridotite and its relation to stress orientations and kinematics of subducting slabs: Insights from the Almirez ultramafic massif. Lithos 320, 470-489.

Elyaszadeh, R., Prior, D.J., Sarkarinejad, K., Mansouri, H., 2018. Different slip systems controlling crystallographic preferred orientation and intracrystalline deformation of amphibole in mylonites from the Neyriz mantle diapir, Iran. Journal of Structural Geology 107, 38-52.

Engelder, T., Geiser, P.A., Alvarez, W., 1981. Role of pressure solution and dissolution in Geology. Geology 9, 44-45.

Fazio, E., Punturo, R., Cirrincione, R., Kern, H., Pezzino, A., Wenk, H.R., Goswami, S., Mamtani, M.A., 2017. Quartz preferred orientation in naturally deformed mylonitic rocks (Montalto shear zone-Italy): a comparison of results by different techniques, their advantages and limitations. International Journal of Earth Sciences 106, 2259-2278.

Fettes, D.J., Desmons, J., Arkai, P., 2011. Metamorphic rocks: a classification and glossary of terms. Recommendations of the International Union of Geological Sciences Subcommission on the Systematics of Metamorphic Rocks. Cambridge University Press.

Godfrey, N.J., Christensen, N.I., Okaya, D.A., 2000. Anisotropy of schists: Contribution of crustal anisotropy to active source seismic experiments and shear wave splitting observations. Journal of Geophysical Research-Solid Earth 105, 27991-28007.

Guo, B.B., Wang, H.C., Zhao, W.H., Ji, S.C., Sun, D.S., Li, A.W., Long, C.X., 2014. Analysis of seismic anisotropy of the typical slate from the Gaoligong mountains, Yunnan province, China. Chinese Journal of Geophysics 57, 154-165.

Hill, R., 1952. The elastic behaviour of a crystalline aggregate. Proceedings of the Physical Society of London Section A 65, 349-355.

Ivankina, T.I., Zel, I.Y., Lokajicek, T., Kern, H., Lobanov, K.V., Zharikov, A.V., 2017. Elastic anisotropy of layered rocks: Ultrasonic measurements of plagioclase-biotite-muscovite (sillimanite) gneiss versus texture-based theoretical predictions (effective media modeling). Tectonophysics 712, 82-94.

Ji, S.C., Wang, Q., Xia, B., 2003. P-wave velocities of polymineralic rocks: Comparison of theory and experiment and test of elastic mixture rules. Tectonophysics, 366, 165-185.

Ji, S.C., Wang, Q., Marcotte, D., Salisbury, M.H., Xu, Z., 2007. P wave velocities, anisotropy and hysteresis in ultrahigh-pressure metamorphic rocks as a function of confining pressure. Journal of Geophysical Research: Solid Earth 112 B9

Ji, S.C., Li, A., Wang, Q., Long, C.X., Wang, H.C., Marcotte, D., Salisbury, M., 2013a. Seismic velocities, anisotropy, and shear-wave splitting of antigorite serpentinites and tectonic implications for subduction zones. Journal of Geophysical Research-Solid Earth 118, 1015-1037.

Ji, S.C., Shao, T.B., Michibayashi, K., Long, C.X., Wang, Q., Kondo, Y., Zhao, W.H., Wang, H.C., Salisbury, M.H., 2013b. A new calibration of seismic velocities, anisotropy, fabrics, and elastic moduli of amphibole-rich rocks. Journal of Geophysical Research-Solid Earth 118, 4699-4728

Ji, S.C., Shao, T.B., Michibayashi, K., Oya, S., Satsukawa, T., Wang, Q., Zhao, W.H., Salisbury, M.H., 2015. Magnitude and symmetry of seismic anisotropy in mica- and amphibole-bearing metamorphic rocks and implications for tectonic interpretation of seismic data from the southeast Tibetan Plateau. Journal of Geophysical Research-Solid Earth 120, 6404-6430.

Johnston, J.E., Christensen, N.I., 1995. Seismic anisotropy of shales. Journal of Geophysical Research: Solid Earth 100, 5991-6003.

Jung, H., 2011. Seismic anisotropy produced by serpentine in mantle wedge. Earth and Planetary Science Letters 307, 535-543.

Kameda, J., Raimbourg, H., Kogure, T., Kimura, G., 2011. Low-grade metamorphism around the down-dip limit of seismogenic subduction zones: Example from an ancient accretionary complex in the Shimanto Belt, Japan. Tectonophysics 502, 383-392.

Kang, H., Jung, H., 2019. Lattice-preferred orientation of amphibole, chlorite, and olivine found in hydrated mantle peridotites from Bjorkedalen, southwestern Norway, and implications for seismic anisotropy. Tectonophysics 750, 137-152.

Keppler, R., 2018. Crystallographic preferred orientations in eclogites - A review. Journal of Structural Geology 115, 284-296.

Kern, H., Lokajicek, T., Svitek, T., Wenk, H.R., 2015. Seismic anisotropy of serpentinite from Val Malenco, Italy. Journal of Geophysical Research-Solid Earth 120, 4113-4129.

Ko, B., Jung, H., 2015. Crystal preferred orientation of an amphibole experimentally deformed by simple shear. Nature Communications 6.

Lonardelli, I., Wenk, H.-R., Ren, Y., 2007. Preferred orientation and elastic anisotropy in shales. Geophysics 72, D33-D40.

Lu, H.J., Hu, D.F., Zhang, R., Li, C.B., Wang, J., Ren, L., 2019. Mechanical behavior investigation of Longmaxi shale under high temperature and high confining pressure. Thermal Science 23, 1521-1527.

Mainprice, D., Bachmann, F., Hielscher, R., Schaeben, H., 2014. Descriptive tools for the analysis of texture projects with large datasets using MTEX: Strength, symmetry and components. Geological Society, London, Special Publications 409.

Mainprice, D., Hielscher, R., Schaeben, H., 2011. Calculating anisotropic physical properties from texture data using the MTEX open-source package, in: Prior, D.J., Rutter, E.H., Tatham, D.J. (Eds.), Deformation Mechanisms, Rheology and Tectonics: Microstructures, Mechanics and Anisotropy, pp. 175-192.

Mainprice, D., Nicolas, A., 1989. Development of shape and lattice preferred orientations - application to the seismic anisotropy of the lower crust. Journal of Structural Geology 11, 175-189.

Meszaros, E., Varga, A., Raucsik, B., Benko, Z., Heincz, A., Hauzenberger, C.A., 2019. Provenance and Variscan low-grade regional metamorphism recorded in slates from the basement of the (SW Hungary). International Journal of Earth Sciences 108, 1571-1593.

Naus-Thijssen, F.M.J., Goupee, A.J., Johnson, S.E., Vel, S.S., Gerbi, C., 2011a. The influence of crenulation cleavage development on the bulk elastic and seismic properties of phyllosilicate-rich rocks. Earth and Planetary Science Letters 311, 212-224.

Naus-Thijssen, F.M.J., Goupee, A.J., Vel, S.S., Johnson, S.E., 2011b. The influence of microstructure on seismic wave speed anisotropy in the crust: computational analysis of quartz-muscovite rocks. Geophysical Journal International 185, 609-621.

Nicolas, A., Boudier, F., Boullier, A.M., 1973. Mechanisms of flow in naturally and experimentally deformed peridotites. American Journal of Science 273, 853-876.

Park, M., Jung, H., 2019. Relationships Between Eclogite-Facies Mineral Assemblages, Deformation Microstructures, and Seismic Properties in the Yuka Terrane, North Qaidam Ultrahigh-Pressure Metamorphic Belt, NW China. Journal of Geophysical Research-Solid Earth 124, 13168-13191.

Passchier, C.W., Trouw, R.A.J., 2005. Microtectonics. Springer-Verlag.

Prior, D.J., Mariani, E., Wheeler, J., 2009. EBSD in the Earth Sciences: Applications, Common Practice, and Challenges, in: Schwartz, A.J., Kumar, M., Adams, B.L., Field, D.P. (Eds.), Electron Backscatter Diffraction in Materials Science. Springer US, Boston, MA, pp. 345-360.

Renedo, R.N., Nachlas, W.O., Whitney, D.L., Teyssier, C., Piazolo, S., Gordon, S.M., Fossen, H., 2015. Fabric development during exhumation from ultrahigh-pressure in an eclogite-bearing shear zone, Western Gneiss Region, Norway. Journal of Structural Geology 71, 58-70.

Reuss, A., 1929. Berechnung der Fließgrenze von Mischkristallen auf Grund der Plastizitätsbedingung für Einkristalle. ZAMM - Journal of Applied Mathematics and Mechanics / Zeitschrift für Angewandte Mathematik und Mechanik 9, 49-58.

Rodríguez-Sastre, M.A., Calleja, L., 2006. The determination of elastic modulus of slates from ultrasonic velocity measurements, 10th IAEG International Congress, Nottingham, p. 11.

Saur, H., Sénéchal, P., Boiron, T., Aubourg, C., Derluyn, H., Moonen, P., 2020. First investigation of quartz and calcite shape fabrics in strained shales by means of X-ray tomography. Journal of Structural Geology 130, 103905.

Sayers, C.M., 2005. Seismic anisotropy of shales. Geophysical Prospecting 53, 667-676.

Seront, B., Mainprice, D., Christensen, N.I., 1993. A determination of the three-dimensional seismic properties of anorthosite: Comparison between values calculated from the petrofabric and direct laboratory measurements. Journal of Geophysical Research: Solid Earth 98, 2209-2221.

Shao, T.B., Ji, S.C., Kondo, Y., Michibayashi, K., Wang, Q., Xu, Z.Q., Sun, S.S., Marcotte, D., Salisbury, M.H., 2014. Antigorite-induced seismic anisotropy and implications for deformation in subduction zones and the Tibetan Plateau. Journal of Geophysical Research-Solid Earth 119, 2068-2099.

Sintubin, M., 1994. Phyllosilicate preferred orientation in relation to strain path determination in the lower Paleozoic Stravelot-Venn Massif (Ardennes, Belgium). Tectonophysics 237, 215-231.

Thomsen, L., 1986. Weak elastic anisotropy. Geophysics 51, 1954-1966.

Valcke, S.L.A., Casey, M., Lloyd, G.E., Kendall, J.M., Fischer, Q.J., 2006. Lattice preferred orientation and seismic anisotropy in sedimentary rocks. Geophysical Journal International 166.

Vasin, R.N., Wenk, H.R., Kanitpanyacharoen, W., Matthies, S., Wirth, R., 2013. Elastic anisotropy modeling of Kimmeridge shale. Journal of Geophysical Research-Solid Earth 118, 3931-3956.

Voigt, W., 1928. Lehrbuch der Kristallphysik: mit Ausschluss der Kristalloptik. B.G. Teubner, Leipzig.

Ward, D., Mahan, K., Schulte-Pelkum, V., 2012. Roles of quartz and mica in seismic anisotropy of mylonites. Geophysical Journal International 190, 1123-1134.

Wenk, H.-R., Kanitpanyacharoen, W., Ren, Y., 2017. Slate – A new record for crystal preferred orientation. Journal of Structural Geology 125, 319-324.

Wenk, H.R., Yu, R., Cárdenes, V., Lopez-Sanchez, M.A., Sintubin, M., 2020. Fabric and anisotropy of slates: from classical studies to new results. Journal of Structural Geology 138, 104066.

Wenk, R., 2012. Texture analysis by advanced diffraction methods, in: Mittemeijer, E.J., Welzel, U. (Eds.), Modern Diffraction Methods. Wiley, pp. 173-220.